CrossMark

RESEARCH PAPER

Multifunctional carbon-coated magnetic sensing graphene oxide-cyclodextrin nanohybrid for potential cancer theranosis

**Yu-Hsuan Hsu · Hui-Ling Hsieh · Geetha Viswanathan · Siew Hui Voon ·
Chin Siang Kue · Wen Shang Saw · Chai Hong Yeong · Che Ahmad Azlan · Toyoko Imae ·
Lik Voon Kiew · Hong Boon Lee · Lip Yong Chung**

Abstract We functionalized graphene oxide (GO) with cyclodextrin (CD) to increase the drug loading and cellular uptake of GO, and bound the GO-CD to carbon-coated iron nanoparticles (Fe@C) with superparamagnetic properties for potential magnetic-directed drug delivery and as a diagnostic agent. The GO-CD/Fe@C was loaded with an anticancer drug, doxorubicin (DOX), to form a multifunctional GO-CD/Fe@C/DOX nanohybrid. A cumulative increase in DOX loading was observed probably due to DOX adsorption to the graphitic domains in Fe@C and also to the GO-CD. In acidic pH that resembles the pH of the tumor environment, a higher amount of DOX was released from the GO-CD/Fe@C/DOX nanohybrid when compared to the amount released at physiological pH. The signal intensity and the contrast enhancement in magnetic resonance imaging of Fe@C decreased with its concentration. Besides, the cellular uptake of GO-CD/Fe@C/DOX nanohybrid was significantly higher by 2.5-fold than that of Fe@C/DOX in MDA-MB-231 human breast cancer model. The nanohybrids were internalized into the tumor cells via an energy-dependent process and localized mainly in the nuclei, where it exerts its cytotoxic effect, and some in the lysosomes and mitochondria. This has resulted in significant cytotoxicity in tumor cells treated with GO-CD/Fe@C/DOX. These findings highlight the potential use of multifunctional GO-CD/Fe@C nanohybrid for magnetic sensing anticancer drug delivery to tumor cells.

Keywords Graphene oxide · Cyclodextrin · Carbon-coated iron · Superparamagnetism · Magnetic resonance imaging · Drug delivery · Nanomedicine

Y.-H. Hsu · H.-L. Hsieh · T. Imae (✉)
Department of Chemical Engineering, National Taiwan University of Science and Technology, 43 Section 4, Keelung Road, Taipei 10607, Taiwan
e-mail: imae@mail.ntust.edu.tw

G. Viswanathan · W. S. Saw · H. B. Lee · L. Y. Chung (✉)
Department of Pharmacy, Faculty of Medicine, University of Malaya, 50603 Kuala Lumpur, Malaysia
e-mail: chungly@hotmail.com
e-mail: chungly@um.edu.my

S. H. Voon · C. S. Kue · L. V. Kiew
Department of Pharmacology, Faculty of Medicine, University of Malaya, 50603 Kuala Lumpur, Malaysia

C. S. Kue
Department of Diagnostic and Allied Health Sciences, Faculty of Health and Life Sciences, Management & Science University, 40100 Shah Alam, Malaysia

C. H. Yeong · C. A. Azlan
Department of Biomedical Imaging, Faculty of Medicine, University of Malaya, 50603 Kuala Lumpur, Malaysia

T. Imae
Graduate Institute of Applied Science and Technology, National Taiwan University of Science and Technology, 43 Section 4, Keelung Road, Taipei 10607, Taiwan

Introduction

Nanoscale drug carriers have emerged as a bridge between nanotechnology and advanced drug delivery,

involving nanomaterials such as liposomes, microspheres, polymeric shells, nanoparticles, carbon nanotubes, and carbon nanohorns (Hubbell and Chilkoti 2012; Voon et al. 2014). For efficient drug action, the amount of drug loaded on these nanomaterials has to be sufficiently high (Viswanathan et al. 2016). Since 2008, many groups have started to explore the use of graphene oxide as high drug loading capacity nanodrug carrier (Kiew et al. 2016). Graphene oxide is an oxidized graphene composed of a graphitic sheet, with two dimensional structures consisting of sp^2-hybridized carbon, exhibiting remarkable electronic and mechanical properties (Zhang et al. 2010). Its one-atom thickness and huge two-dimensional plane give graphene oxide a large specific surface area. As a result, drugs can be loaded on the graphene sheet through π-π stacking, covalent binding, and hydrophobic or electrostatic interaction (Liu et al. 2008; Zhang et al. 2010). In addition, graphene oxide is pH-sensitive giving higher drug release at tumoral acidic pH and possesses good water dispersibility (Kiew et al. 2016).

Functionalization of GO with active targeting ligands including folic acid (Yang et al. 2011; Zhang et al. 2010), transferrin (Liu et al. 2013), and Asn-Gly-Arg peptide (Shi et al. 2014) has been reported to enhance tumor targeting and accumulation of the GO at tumor sites. However, these ligand-conjugated GO generally possess limited ability to access and penetrate solid tumor effectively (Brumlik et al. 2008; Das et al. 2009). Moreover, receptor heterogeneity, lack of information on the rate of ligand-receptor binding, rate of receptor recycling, and downregulation of receptor due to receptor saturation result in elevated toxicities and reduce therapeutic efficacies (Bandara et al. 2014; Kue et al. 2016; Paulos et al. 2004). These lead to challenges in choosing the perfect ligand and selecting the dosing that delivers consistent pharmacokinetics (Das et al. 2009).

To overcome these hurdles, magnetic targeted nanomaterial has emerged as an alternative for tumor-selective delivery and attracted great interest in the field of drug delivery in recent years (Chomoucka et al. 2010; Mody et al. 2013). Many studies have shown that magnetic nanoparticles can be accumulated and retained at tumor sites by a locally applied external magnetic field (Fernández-Pacheco et al. 2005). This magnetic tumor targeting has the advantage over active targeting using antibody or ligands because they are independent of tumor cell types and receptors (Alexiou et al. 2000;

Bae et al. 2012; Fernández-Pacheco et al. 2005). The drugs adsorbed or chemically bonded to the magnetic particles will reach the targeted site and eventually desorbed on the tumor area over a prolonged period of time with the aid of an external magnet (Alexiou et al. 2000; Fernández-Pacheco et al. 2005). This will increase the accumulation of the drug at the tumor site, improve the efficacy of chemotherapy, and reduce systemic toxicity.

However, magnetic iron nanoparticles are prone to oxidation, affecting their stability, magnetic properties, and biocompatibility (Aguiló-Aguayo et al. 2010). To circumvent this, carbon coating can be applied to iron nanoparticles to provide an oxidation barrier and prevent corrosion of the magnetic core materials besides reducing interactions between the particles (Bae et al. 2012). The carbon coating will also improve the particle dispersibility and stability due to its hydrophilicity, rendering the iron particles biologically inert (Bae et al. 2012; Fernández-Pacheco et al. 2005). Drug loading can be increased because carbon surfaces are effective for physical adsorption of drugs (Rudge et al. 2000; Terzyk 2001). Moreover, magnetic nanoparticle is potentially amenable to hyperthermia therapy, where upon appropriate electromagnetic irradiation, it is activated and then releases vibrational energy in the form of heat to kill the target cells at the vicinity (Kobayashi et al. 2014).

Taking advantage of the superparamagnetic property of carbon-coated iron nanoparticles (Fe@C) and the high drug loading capacity of graphene oxide-cyclodextrin (GO-CD), carbon-coated iron-bound graphene oxide-cyclodextrin (Fe@C-bound GO-CD) nanohybrids were prepared as drug carriers for potential magnetic-directed drug delivery and magnetic resonance imaging (MRI). Doxorubicin, an effective antineoplastic chemo drug routinely used in breast cancer treatment (Cortés-Funes 2007), was loaded on Fe@C-bound GO-CD. Herein, we reported the synthesis and characterization of doxorubicin (DOX)-loaded Fe@C-bound GO-CD, as well as evaluation of Fe@C-bound GO-CD/DOX nanoparticle's drug release and cytotoxicity profiles, cellular uptake, and localization in MDA-MB-231 human breast cancer cells, for its potential as a multifunctional carbon-coated magnetic-directed nanohybrid for cancer theranosis (combined therapy and diagnosis).

Experimental procedures

Reagents and instruments

Ethylenediamine, *p*-toluenesulfonyl chloride (TsCl), *N*-hydroxysuccinimide (NHS), and 1-ethyl-3-(3-dimethylaminopropyl) carbodiimide (EDC) were purchased from Sigma-Aldrich (USA). Sodium borohydride and β-cyclodextrin (CD) were purchased from Wako. Citric acid and iron chloride hexahydrate were purchased from Acros Organics (USA). Graphene oxide (GO) was purchased from UniRegion Bio-Tech Corp. (USA). DOX was kindly donated by Prof. H. C. Tsai, National Taiwan University of Science and Technology, Taiwan. Other chemicals were of commercial grade. All reagents were used without further purification. Ultrapure water (Yamato Millipore WT100, resistivity of 18.2 MΩ cm^{-1}) was used throughout the whole solution preparation.

The dynamic light scattering (DLS) was recorded by a Horiba SZ-100 scientific. Magnetization was measured using TM-VSM151483N7-MRO (Tamakawa Co., Japan) at room temperature. X-ray diffraction (XRD) patterns were obtained with a Bruker D2-phaser diffractometer using CuKα radiation (λ = 1.5418 Å). High-resolution transmission electron microscopic (HR-TEM) images and EDX spectra were obtained on Philips/FEI Tecnai 20 G2 S-Twin. Fourier transform-infrared (FT-IR) absorption spectra were obtained for KBr disc on a Thermo Scientific Nicolet 6700 FTIR spectrometer. The thermogravimetric analysis (TGA) was performed by using a TA Q500 instrument at the flow rate of N$_2$ at 60 ml/min, temperature up to 800 °C, and constant rate of 20 °C/min. The morphology observation was performed using transmission electron microscope (TEM, Hitachi H-7000 and HT7700, Tokyo, Japan) at the acceleration voltage of 100 kV.

Synthesis of β-CD-conjugated GO (GO-CD) and carbon-coated iron nanoparticles (Fe@C)-bound GO and GO-CD (GO-Fe@C, GO-CD-Fe@C)

Aminated β-CD (amino-β-CD) was synthesized through tosylation and amination processes following a previous report (Ohashi et al. 2006). In brief, β-CDs (2 g) and *p*-TsCl (1.5 g) at mole ratio of 1:5 (CD:TsCl) were reacted in an aqueous NaOH solution (0.4 M, 30 ml) for 1.5 h at 0 °C under vigorous stirring. After unreacted solid TsCl was removed by filtration, the

solution was then adjusted to pH 7 using hydrochloric acid to yield the precipitated tosyl-β-CD. The crude precipitate separated by filtration was recrystallized from hot water (20 ml, 90 °C).

Tosyl-β-CD (15.5 g) was then dissolved in ethylenediamine (180 ml) and refluxed at 40 °C for 24 h under stirring. The unreacted ethylenediamine was evaporated using a rotary evaporator and the condensed solution was dropped into acetone (700 ml) and stirred overnight. The resultant precipitate was recrystallized from a mixture of methanol and water (3:1 volume ratio) and followed by acetone.

Fe@C was synthesized by the hydrothermal carbonization method (Prasannan and Imae 2013). Iron chloride hexahydrate (0.25 g) in ethanol (30 ml) and sodium borohydride (0.38 g) in water (30 ml) were mixed and the solution was stirred for 15 min. A mixture of citric acid (1 g), ethylenediamine (0.3 ml), and water (10 ml) was then added and heated for 5 h at 250 °C in an autoclave. The product was collected by magnet and washed with water. Carbon dots were also synthesized by the same procedure without addition of iron chloride hexahydrate in ethanol and sodium borohydride in water. The synthesis of bare iron particles without carbon coating was performed from the mixture of only iron chloride hexahydrate in ethanol and sodium borohydride in water (Himaja et al. 2015; Krishnakumar et al. 2014).

Size-controlled GO nanosheet was prepared by mechanically fragmenting commercial GO (550 nm) in water by a sonicator (QSONICA, Q700) with a ½-in. horn tip at 50 mA for 4 h in an ice bath and collected by filtration using cellulose acetate membrane filter with 0.2 μm pore size (Siriviriyanun et al. 2015). The average hydrodynamic size of GO nanosheet evaluated from DLS was 100 nm. A carboxylate group on GO was bound with an amine group on amino-β-CD using condensing agents EDC and NHS (equimole to amino-β-CD) according to the conventional amidation procedure (Konkena and Vasudevan 2012a; Paredes et al. 2008; Siriviriyanun et al. 2015). Fe@C-bound GO and Fe@C-bound GO-CD were also synthesized by the same amidation reaction. An aqueous dispersion of carboxylate-possessing compound (GO or GO-CD) was mixed with equimolar EDC and NHS and stirred for 24 h at room temperature; after amine-possessing compound (amino-β-CD or Fe@C) was added, the mixture was further stirred for 24 h at room temperature. The products were purified by dialysis or centrifugation

(cellulose tubular dialysis membrane MCWO 6000–8000) or centrifugation (135,000 rpm).

Loading and release of DOX on nanocarriers and in vitro cytotoxicity assay of DOX-loaded nanocarriers

Loading of DOX on nanocarriers (GO and GO-CD, Fe@C, GO-Fe@C, and GO-CD-Fe@C) was carried out by mixing an aqueous suspension of nanocarrier with DOX at different DOX concentrations (Siriviriyanun et al. 2015). The mixture was sonicated and stirred overnight at room temperature in the dark, and unbound DOX was removed by centrifugation (135,000 rpm). The concentration of unbound DOX in the supernatant was determined from absorbance at a spectroscopic absorption band of DOX (480 nm), and the amount of loaded DOX was evaluated as a difference of the amount of unbound DOX from the initial amount of DOX.

For the release experiment of DOX, an aqueous dispersion of DOX-loaded nanocarrier in a dialysis membrane tube (molecular weight cutoff (MWCO) = 6000–8000) was dialyzed under continuous stirring in water at pH 5 and 7 at room temperature. Then, the amount of DOX released from the carrier was determined following the spectrometric method.

Magnetic resonance imaging

Fe@C was suspended in 2% *w/v* agar solution in a concentration ranging between 0.06 and 20 mM of Fe equivalent. MRI images were acquired using a 3-T MRI system (Magnetom Prisma, Siemens Healthcare, Erlangen, Germany). The transverse relaxation time (T_2) for each Fe@C concentration was determined by acquisition of coronal images at various echo times (TE) ranging from 55 to 155 ms with a repetition time (TR) of 5200 ms. Region of interest (ROI) was placed at the MRI image of each sample to obtain the signal intensity. Mono-exponential curve fitting of the plots of signal intensity versus TE was done using Matlab software (Matlab R2016b, MathWorks, Natick, MA). The relaxation rate, R_2 ($1/T_2$), was calculated using the following equation:

$$S = S_0 \left[e^{-\frac{TE}{T_2}} \right] + C$$

Where S is the signal intensity at time (TE), S_0 is the maximum signal achievable, and C is the noise level. The

R_2 values obtained were then plotted against the different Fe concentrations and the slope of the curve indicates the T_2 relaxivity, which is a measure of the sensitivity of a formulation for negative contrast enhancement.

Cellular uptake of DOX-loaded nanocarriers by flow cytometry and by confocal microscopy

For flow cytometry, cells (1.5×10^5 cells/well) in 12-well culture plates were incubated as described above and further incubated with DOX-loaded nanocarriers (10 μg/ml DOX equivalent) or free DOX (10 μg/ml) for 2 h. The treated cells were washed, trypsinized, and centrifuged. The cells were resuspended in PBS (0.5 ml) containing fetal bovine serum (FBS) (0.5%) and used for flow cytometric analysis on a BD FACS Canto II flow cytometer (Becton Dickinson, San Jose, USA) equipped with a 488-nm argon laser and a 670-nm long pass filter. Data from 10,000 cells were analyzed using FACS DIVA analysis software (Becton Dickinson).

For confocal microscopic observation, after cells were cultured with DOX-loaded nanocarriers as described above, cells were fixed on glass coverslips and mounted on glass slides with mounting medium containing 4′,6-diamidino-2-phenylindole (DAPI) (Slow Fade Gold Antifade Mount, Life Technologies Inc., Carlsbad, USA). On the observation with a confocal laser scanning microscope using a ×63 oil immersion objective (Leica TCS SP5 II, Leica Microsystem, Wetzlar, Germany), the excitation and emission wavelengths for DAPI were 405 and 414–481 nm, and for DOX were 488 and 590–720 nm, respectively. Images were captured using the Leica LAS-AF image capture software, and the fluorescence intensity of DOX was analyzed using Leica Application Suite-X (LAS-X) software (Busquets et al. 2010; Fan et al. 2013).

To assess the effect of low temperature on the uptake of GO-CD/DOX, GO-CD-Fe@C/DOX, and Fe@C/DOX, flow cytometric cellular uptake studies were repeated based on the procedures described above, except that cells were treated with GO-CD/DOX, GO-CD-Fe@C/DOX, and Fe@C/DOX for 2 h at 4 and 37 °C, respectively.

Intracellular localization of GO-CD/DOX, GO-CD/Fe@C/DOX, and Fe@C/DOX

The analysis of the intracellular localization was carried out for dual staining cells on a confocal microscope, as

described previously (Viswanathan et al. 2016). In brief, MDA-MB-231 cells grown on coverslips in 6-well plates were incubated with test samples for 2 h, as described in the confocal cellular uptake studies above. The cells were then rinsed twice with PBS to remove free nanocarrier/DOX. Subsequently, the cells were stained with organelle-specified fluorescence probe (100 nM), that is, with MitoTracker green, ER-Tracker blue-white DPX, and LysoTracker blue for mitochondria, endoplasmic reticulum, and lysosomes, respectively. The co-localization of nanocarriers was examined using DOX fluorescence. Cells were incubated with each stain for 30 min at room temperature, rinsed with PBS, and observed by a confocal microscope. The excitation and emission wavelengths were 405 and 414–481 nm for both LysoTracker and ER-Tracker and 488 and 494–524 nm for MitoTracker green. All scans were performed with an independent sequential mode; hence, there was no spectral overlap in the acquisition. The intracellular localization of the test samples was determined by comparing the fluorescence topographic profile of each organelle probe generated from a longitudinal transcellular axis.

In vitro cytotoxicity assay

In vitro cytotoxicity assay was carried out following a previously reported procedure (Viswanathan et al. 2016). In brief, MDA-MB-231 cell line was grown and maintained in Dulbecco's modified Eagle's medium (DMEM) supplemented with 10% FBS and 1% penicillin-streptomycin at 37 °C in a 5% CO_2 humidified chamber. Cells were seeded into 96-well plates at 5000 cells/well and were incubated overnight to allow cells to adhere. DOX-loaded nanocarriers were diluted in culture medium and added to the cells to give final concentrations. The cells were then incubated for 24 h at 37 °C in 5% CO_2.

The cell viability was assessed by adding 10 μl of 3-(4,5-dimethylthiazol-2-yl)-2,5-diphenyl tetrazolium bromide (MTT) (5 mg/ml in PBS) to each well and incubated for 3 h. After removal of the supernatant, the purple formazan crystal was dissolved by adding 100 μl of dimethylsulfoxide. The cell viability was calculated from the optical density of each well read by a microplate reader.

Results and discussion

### Characterization of Fe@C and Fe@C-bound GO

The magnetic properties of Fe@C were demonstrated when the well-dispersed Fe@C in water (Fig. 1a) was fully directed by a magnet (Fig. 1b), and the Fe@C redispersed in water upon removal of the magnet. When the hysteresis loop of magnetization of Fe@C was measured at room temperature, the result indicated that the remanence and coercivity were close to zero suggesting that it displayed the characteristics of superparamagnetism (Wang et al. 2015a). The saturation magnetization of Fe@C was at 2.45 emu/g (Fig. 1c) which is lower compared to bulk Fe_2O_3 (Popplewell and Sakhnini 1995). The reduction in magnetization value might be attributed to the Fe in nanosize and the coating of nanoparticles with nonmagnetic materials (Tourinho et al. 1989). Despite that, Fe@C could be directed under the action of an external magnet and can be used for targeting drug delivery.

Figure 2 shows the powder XRD pattern of Fe@C. Broad peaks at 45° and 60° corresponded to (110) and (200) indices of Fe^0, indicating that the zero valent iron is present in this powder (Shen et al. 2010; Sun et al. 2006). Incidentally, bare iron without protection by carbon was easily oxidized and became a mixture with
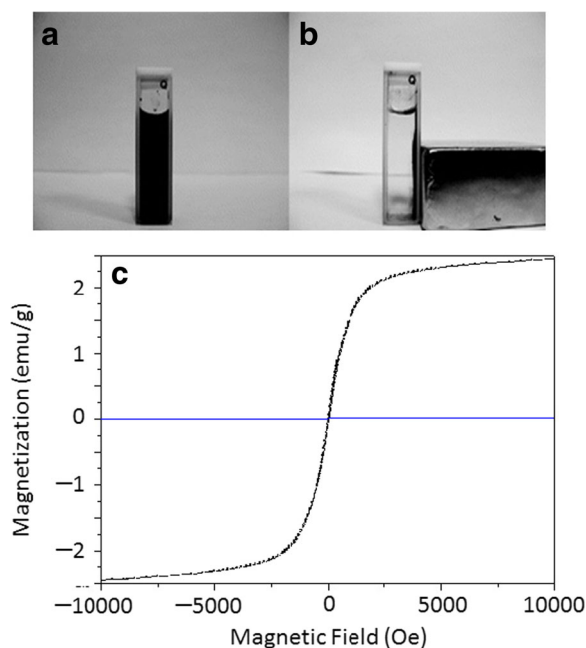

Fig. 1 Magnetic property of Fe@C **a** without magnet, **b** with magnet, and **c** magnetization of Fe@C
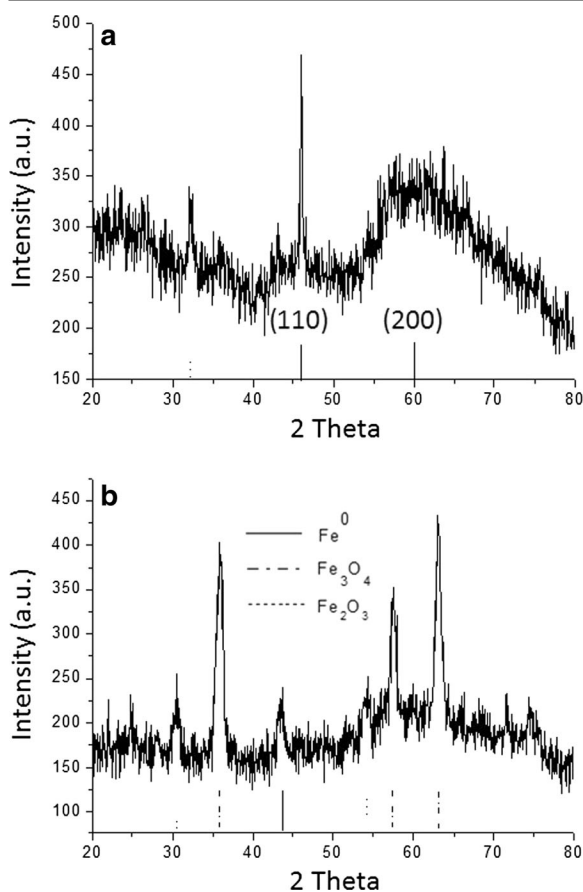
Fig. 2 XRD spectra of **a** Fe@C and **b** iron particles without carbon coating

Fe_3O_4 and Fe_2O_3. The XRD results prove that carbon-coated iron is not oxidized; in other words, iron coated by carbon is protected from air oxidation. Thus, the synthesis of Fe nanoparticles by chemical reduction method follows the equation:

$$2FeCl_3 + 6NaBH_4 + 18H_2O \rightarrow 2Fe^0 + 6NaCl$$
$$+ 6B(OH)_3 + 21H_2$$
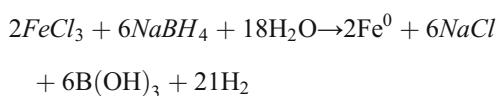
HR-TEM observation (Fig. 3) of Fe@C revealed that Fe particles were found to be spherical of about 5 nm diameter and formed by a single crystalline domain. The two repeating distances in the crystal were 0.25 and 0.20 nm, and these values were consistent with the observation of (110) and (200) indices of Fe in XRD. Thus, it is confirmed from the EDX data in Fig. 3 that the peaks of Fe in Fe@C were much weaker than the peak of carbon, because the carbon component was

more dominant than the Fe component. Cu peaks were from the copper substrate.

On TGA data in Fig. 4, the weight loss curve of carbon dots exhibited mass loss of 7.2–10.0 wt% at 40–200 °C due to the loss of moisture in the nanoparticles. In the temperature interval at 350–500 °C, the mass loss was attributed to the decomposition of organic components in carbon dots. The last weight loss nearly started around 550 °C might be the decomposition of the residual carbon, since there was no obvious weight loss at the temperature higher than 680 °C.

The weight loss of Fe@C also occurred at three steps: It began at 40–150 °C due to the loss of moisture. In the temperature interval at 150–300 °C, the mass loss corresponded to the decomposition of the components in carbon. In the temperature interval of 350–500 °C, weight loss of 20% was attributed to the remaining carbon components in Fe@C. Besides, the carbon components were burned off until 550 °C, and the unburned components of 25.7% remained, being attributed to the iron components.

The morphology of GO, GO-CD, Fe@C, and GO/Fe@C was characterized by using TEM (Fig. 5). GO can be clearly seen as single flat sheets, while other hybrids (GO-CD and GO/Fe@C) exhibited folds or accumulation of GO sheets as evidenced by darker contrast in TEM images. On the other hand, Fe@C nanoparticles aggregated into a cluster.

Table 1 lists the FTIR absorption bands of carbon dots, Fe@C, Fe@C-bound GO, and GO and their assignments. The IR absorption bands of carbon dots and Fe@C were similar to each other as Fe is not detectable in the observed region. The band at 1643 cm^{-1} could be ascribed to carbon-carbon stretching vibration mode of polycyclic aromatic hydrocarbons (Narayanan et al. 2012), and the band at 1584 cm^{-1} was attributed to amine bending mode overlapped with carboxylate antisymmetric stretching mode (Vermisoglou et al. 2014). The band at 1380 cm^{-1} is likely to be the overlapping of stretching mode of polycyclic aromatic hydrocarbons and carboxylate symmetric stretching mode (Jusin et al. 2016). In the spectrum of GO, a weak IR band at 1736 cm^{-1} is associated with carbonyl stretching vibration from the oxidized groups in graphene, and IR bands at 1623 and 1366 cm^{-1} are attributed to polycyclic aromatic hydrocarbons in graphene (Paredes et al. 2008; Yu et al. 2010). For Fe@C-bound GO, the three main adsorption bands at 1700~1300 cm^{-1} from Fe@C and GO were commonly observed (Jusin et al. 2016; Ma

**Fig. 3** **a** TEM images. **b** EDX spectrum of Fe@C
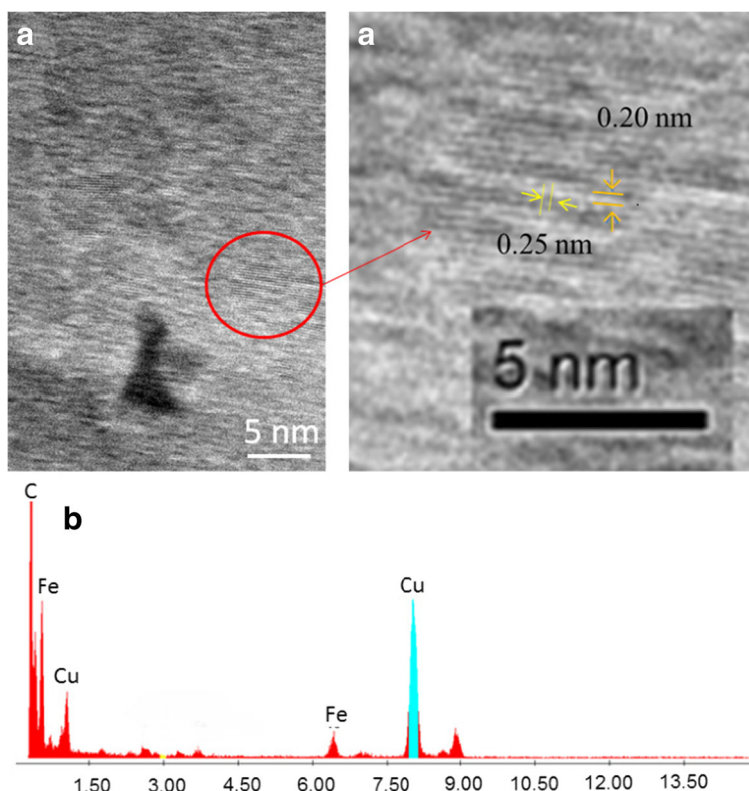
et al. 2012). The only difference is the absence of carbonyl group in GO, because carboxylic acid in GO was exhausted in the amidation reaction with the amine group of Fe@C. The IR absorption bands of the produced amide group may be overlapped on bands of aromatic and amine (+ carboxylate) groups.

The UV-vis absorption spectra and zeta potential were measured for aqueous dispersions of Fe@C, GO, and Fe@C-bound GO and listed in Table 2. The GO has a strong absorption band at 243 nm and a shoulder band at 312 nm, while the Fe@C displayed a shoulder band at 259 nm and a band at 352 nm. After amidation between GO and Fe@C, Fe@C-bound GO had weak shoulder bands at 267 and 334 nm. The zeta potential values of GO, Fe@C, and Fe@C-bound GO were -67, -39, and -56 mV, respectively. Overall, the negative surface charges of these samples could be attributed by the presence of carboxylate groups. The decrease in the number of carboxylate groups on GO due to the amidation reaction might be the possible explanation for the reduction of negative charge in Fe@C-bound GO.

In vitro DOX loading on GO, GO-CD, Fe@C, and GO-CD/Fe@C/DOX nanohybrid

Composites of CD and Fe@C with GO developed in this study may serve as promising multifunctional nanoplatforms for magnetic drug delivery of anticancer drugs. Thus, the loading of DOX on different carriers was examined by adding DOX to aqueous dispersions of carriers: GO, GO-CD (GO:CD = 1:1 and 1:10 (weight ratio)), Fe@C, GO/Fe@C (GO:Fe@C = 1:1 (weight ratio)), and GO-CD/Fe@C (GO:CD:Fe@C = 1:1:1 (weight ratio)), and the amounts were evaluated at different added concentrations of DOX (0.4, 0.8, and 2.0 mg/ml). The numerical values of loading amounts are listed in Table 3, and their graphical comparison is shown in Fig. 6. The loading of DOX on nanocarriers increased in parallel with increasing added concentration of DOX, indicating that there was a dose-dependent increase in uptake.

Functionalization of CD on GO and the increasing amount of CD on GO influenced the loading amount of DOX, namely, the loading amount increased in the order of GO < GO-CD(1:1) < GO-CD(1:10), because CD has
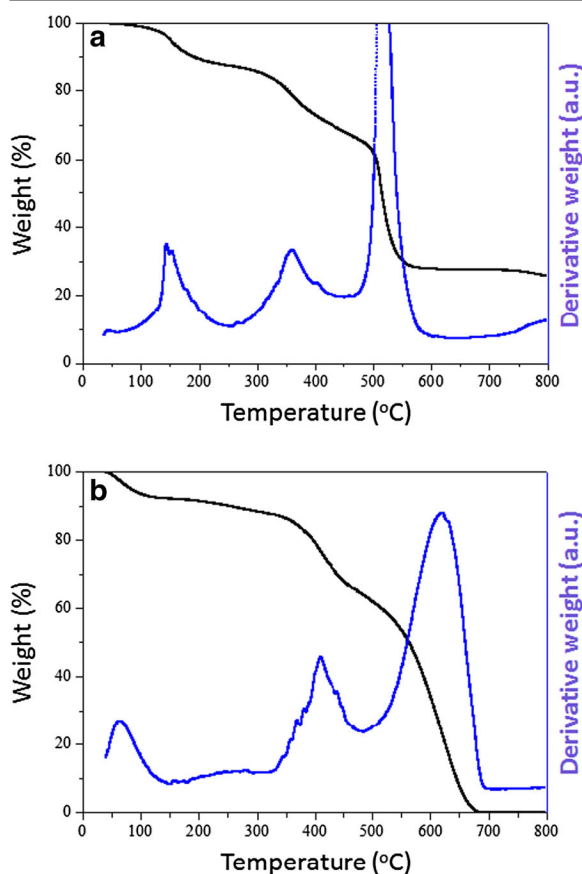
**Fig. 4** TGA curves of **a** Fe@C and **b** carbon dots

a cavity to host a DOX molecule. This can be ascribed to the superimposition of CD cavities on GO that resulted in the additional DOX loading capacity.

Fe@C itself was capable of being loaded with DOX, because it possesses graphitic domains to enable the adsorption of DOX, although the loading amount of DOX on Fe@C was lower than that on GO, which depended on the size of the graphitic domains (see

Table 3 and Fig. 6). When Fe@C was chemically bound to GO, the DOX loading was relatively higher than those on Fe@C and GO, individually. Moreover, the coexistence of CD with GO and Fe@C cumulatively increased the loading amount of DOX. This resulted in the highest DOX loading in Fe@C-bound GO-CD nanohybrid. This suggest that GO, CD, and Fe@C possess respective adsorption sites for DOX and the combined effect of each site is likely to be additive instead of synergistic, because each individual binding site is discrete and isolated from each other.

In vitro DOX release from GO-CD, Fe@C, and GO-CD/Fe@C nanohybrids

The release behavior of DOX from the nanocarriers was investigated at pH values 5 and 7, corresponding to the different microenvironments of the tumor cells (lower pH at 5) compared with the normal cells (higher pH at 7) (Tannock and Rotin 1989; Wang et al. 2015b). As seen in Fig. 7, DOX was released from GO and GO-CD nanocarriers, and the release rate gradually declined after 8 h. The total amount of DOX released at the acidic condition was always higher than that at the neutral condition. A similar time dependence was observed for the DOX released from Fe@C, Fe@C-bound GO, and Fe@C-bound GO-CD under the neutral and acidic environments. These behaviors are reasonable and necessary for effective chemotherapy. Another noteworthy result is the similarity of the DOX release in percentage: The release of bound DOX within 48 h was about 20% at pH 7 for all carriers and about 35% at pH 5 for GO and GO-CD carriers. However, in the case of the Fe@C series, the release varied slightly from Fe@C (32%), Fe@C-bound GO (35%) to Fe@C-bound GO-CD (38%) (see Table 3). Furthermore, the total amount of released DOX should be
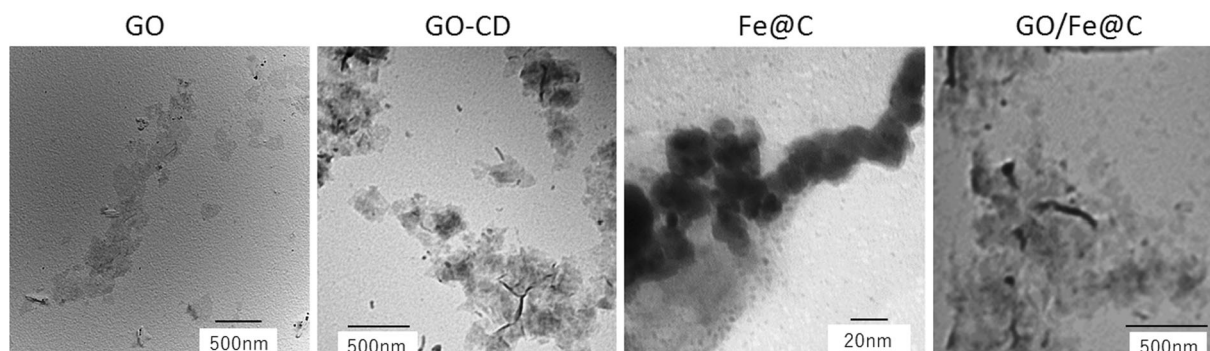
Fig. 5 Microscopic characterization. TEM images of GO, GO-CD, Fe@C, and Fe@C-GO

Table 1 FT-IR absorption bands and their assignments of carbon dots, Fe@C, Fe@C-bound GO, and GO

IR band (cm^{-1})	Carbonyl	Aromatic	Amine + carboxylate	Aromatic + carboxylate
Carbon dots		1620	1563	1380
Fe@C		1643	1584	1376
GO/Fe@C		1642	1593	1354
GO	1736	1623		1366
GO-CD	1735, 1701	1636		1400

compared. As seen in Table 3, the release increased with increasing loading amount, that is, in the order of GO < GO-CD(1:1) < GO-CD(1:10) and Fe@C < GO/Fe@C < GO-CD(1:1)/Fe@C.

The DOX loading and release behavior may reflect the difference between the binding site on GO, CD, and Fe@C and the binding constant of DOX on these sites. Among these three binding sites of DOX, CD possesses a hydrophobic cavity to host lipophilic guests and thus make an inclusion compound with DOX. Therefore, the loading amount increases with increasing CD content. GO and Fe@C have graphene domains and graphenized structure, respectively, which are adequate for π-π stacking with aromatic domain in DOX. In addition, the carboxylate from the oxidized functional groups in GO can form electrostatic interactions with the amine group in DOX. Meanwhile, the graphenized structure in Fe@C does not have the additional stabilization by such electrostatic interaction with DOX, therefore resulting in the inferior loading on Fe@C compared to GO.

DOX has a pKa of 8.2 and the amine in DOX is protonated in neutral and acidic conditions, whereas GO has a main pKa at 6.6 and the carboxylate groups in GO keeps their anionic character at pH higher than 6.6 (Konkena and Vasudevan 2012b). Thus, DOX interacts with GO by the electrostatic interaction with carboxylate groups besides the π-π stacking attraction at neutral

condition. Conversely, at acidic condition below pH 6.6, the electrostatic interaction between DOX and GO will diminish due to the protonation of carboxylates, hence leading to the release of DOX. This might explain why the nanohybrids had higher amount of DOX release in acidic environments compared to neutral condition.

Magnetic resonance imaging of Fe@C

Figure 8a shows MRI images of Fe@C of varied concentrations in the agar gel. It was noted that the signal intensities of the samples decreased with increasing concentration of Fe. This was also clearly shown in the relaxation curve (Fig. 8b) where the slope was less steep when the Fe concentration increased. Signal enhancement can be calculated using the following formula:

$$Enhancement = \left[\frac{SI_{Fe@C} - SI_{blank}}{SI_{blank}} \right] \times 100$$

Table 2 UV-visible absorption bands and zeta potentials of carbon Fe@C, Fe@C-bound GO, and GO

	UV-visible band (nm)		Zeta potential (mV)
Fe@C	259	352	− 39
GO/Fe@C	265	334	− 56
GO	243	312	− 67
GO-CD	240	300	− 62

Table 3 Amount of DOX loaded on various carriers and released from carriers

Carrier (0.1 mg/ml)	Loading (g/g carrier)			Release[a] (g/g carrier)	(wt%)
	DOX added (mg/ml)				
	0.4	0.8	2.0		
GO	1.46	2.01	2.36	0.70	35
GO-CD (1:1)	2.23	2.49	2.74	0.87	35
GO-CD (1:10)	3.15	3.32	3.57	1.16	35
Fe@C	1.00	1.76	2.03	0.56	32
GO/Fe@C (1:1)	1.73	2.41	2.58	0.84	35
GO-CD/Fe@C (1:1:1)	2.61	3.16	3.50	1.20	38

[a] Release from DOX loading at a DOX concentration of 0.8 mg/ml

Fig. 6 Loading amount of DOX **a** on GO and GO-CD (1:1, 1:10 (g/g)) and **b** on Fe@C, GO/Fe@C, and GO-CD(1:1)/Fe@C
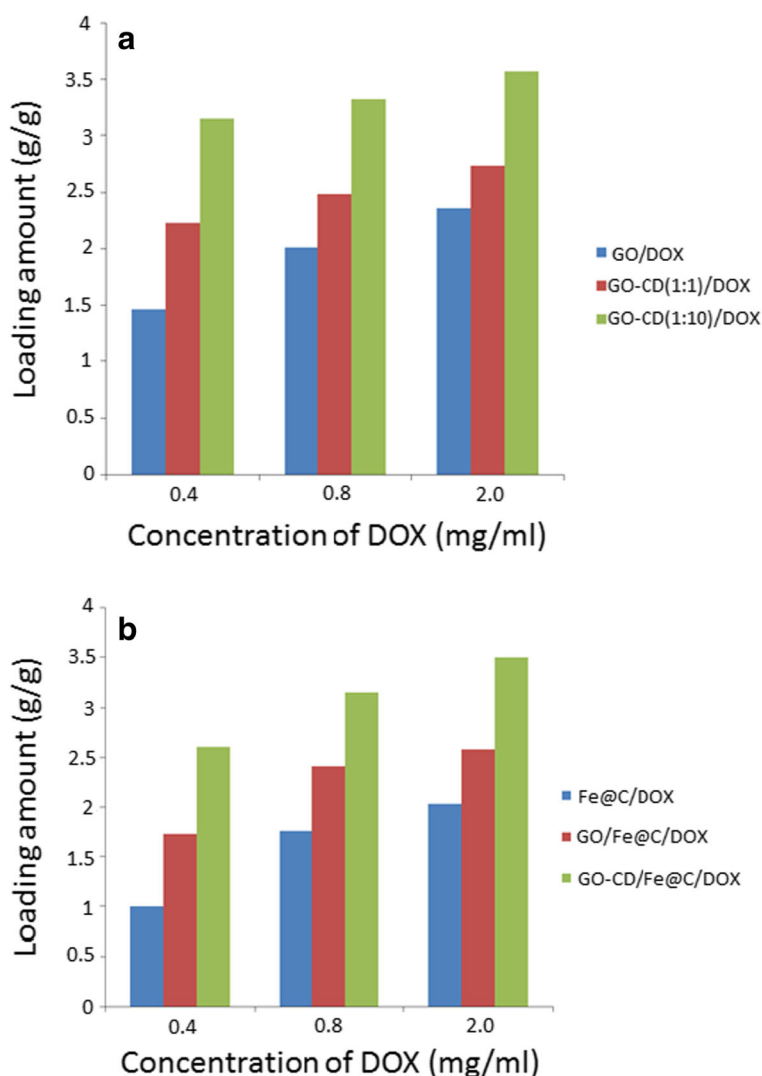

where $SI_{Fe@C}$ is the MRI signal intensity from agar gel containing Fe@C and SI_{blank} is the signal intensity from the agar gel only.

At a concentration of 0.06 mM Fe (3.4 μg ml^{-1} Fe), the contrast enhancement was −13.8%, while at the highest concentration, 2.0 mM Fe (111.6 μg ml^{-1} Fe), the contrast enhancement was −89.2%. For 20.0 mM Fe@C, the signal intensity was equivalent to the background, and hence, this sample was excluded from the T_2 relaxivity analysis. Overall, contrast enhancement is corresponding to the increase of the concentration of Fe@C, which suggests that Fe@C can be used as MR contrast agent.

T_2 relaxivity (from the slope of the graph shown in Fig. 8c) was found to be 9.37 mM^{-1} s^{-1}, which is lower than commercial formulations like the carboxydextran-coated Resovist® (151.0 mM^{-1} s^{-1}) (Mahajan et al. 2013). However, our value was higher compared to carbon-coated iron oxide reported by Bae et al. (2012), which is at 1.115 mM^{-1} s^{-1} (Bae et al. 2012). The presence of Fe@C generates an additional magnetic field to induce disturbance in the local field that significantly increases the speed of proton transverse relaxation and hence decrease in T_2, leading to image darkening or negative contrast. By incorporating Fe@C on GO-CD, GO-CD/Fe@C might behave as a potential theranostic agent. The evaluation of Go-CD/Fe@C in

Fig. 7 The release of DOX **a** on GO and GO-CD (1:1, 1:10) and **b** on Fe@C, Fe@C-bound GO, and Fe@C-bound GO-CD at different pH values
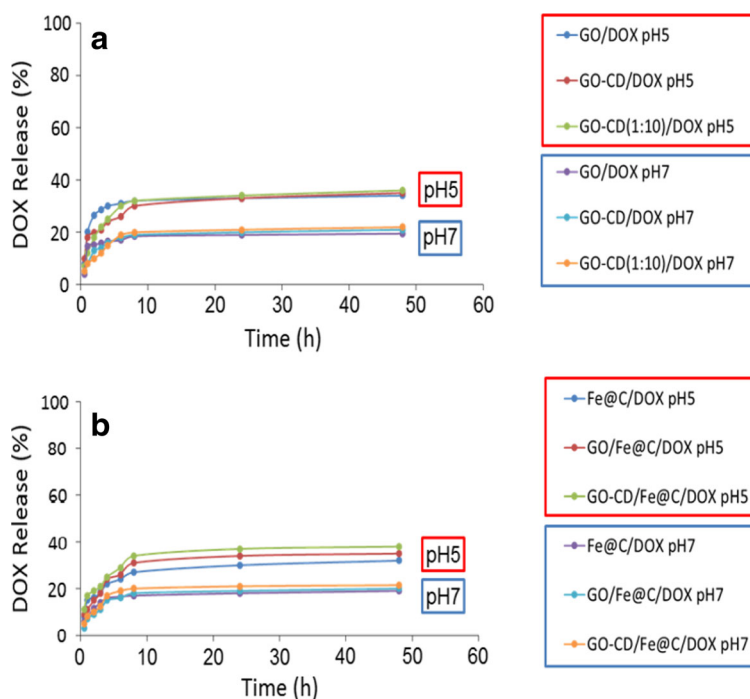
MRI will be emphasized and included in our future study.

### Cellular uptake of GO-CD, Fe@C, and GO-CD/Fe@C nanocarriers

Cellular uptake of GO-CD, Fe@C, and GO-CD/Fe@C nanocarriers in MDA-MB-231 cancer cells was evaluated based on the fluorescence of DOX loaded in the carriers using flow cytometry (Fig. 9). After 2 h incubation, GO-CD/DOX- and GO-CD/Fe@C/DOX-treated cells showed DOX fluorescence in 96 and 97% of the cells, respectively. However, only 38.5% of Fe@C/DOX-treated cells emitted DOX fluorescence (Fig. 9a). Similarly, the mean fluorescence intensity was the lowest for Fe@C/DOX compared to GO-CD/DOX and GO-CD/Fe@C/DOX in cancer cells treated with 0.5–10 μg/ml DOX equivalence (Fig. 9b). The low cellular uptake of Fe@C/DOX could conceivably be due to the nature of iron nanoparticles to form cluster-like aggregates (Rosická and Šembera 2011; Wang et al. 2015a) and thereby reduced uptake by cells. The adsorption of positive-charged DOX on the surface of Fe@C (Nawara et al. 2012) might also shield Fe@C surface charge and promote their aggregation. The intensity for GO-CD/Fe@C/DOX-treated cells was higher than that of GO-CD/DOX and increased with the concentration of DOX.

These results indicate that the uptake of Fe@C by tumor cells has increased upon conjugation with GO-CD. The similar amount of cellular uptake between GO-CD/Fe@C and GO-CD suggests that conjugation of GO-CD with Fe@C enabled favorable uptake of GO-CD/Fe@C by tumor cells, which is vital for chemotherapeutic drug delivery, in addition to the increased drug loading as discussed above. This finding is also supported by 99% uptake of FGA-labeled GO-CD observed in HeLa and MDA-MD-231 cells using flow cytometry (data not shown).

The flow cytometry-based results of GO-CD, Fe@C, and GO-CD/Fe@C nanocarrier uptake were in agreement with the findings from confocal microscopy. The red fluorescence of DOX observed in the MDA-MB-231 cells treated with GO-CD/DOX and GO-CD/Fe@C/DOX was stronger than that in cells treated with Fe@C/DOX (Fig. 9c). The DOX red fluorescence co-localized favorably at high intensity with the blue fluorescence in the nuclear compartment. Meanwhile, some red fluorescence was also found in the cytoplasm (Fig.

Fig. 8 **a** Magnetic resonance imaging of Fe@C of varying concentrations in agar gel (TE = 77 ms; TR = 5200 ms). **b** T_2 relaxation analysis curves. **c** The plot of transverse relaxation rate ($1/T_2$) versus different concentrations of Fe (mM)
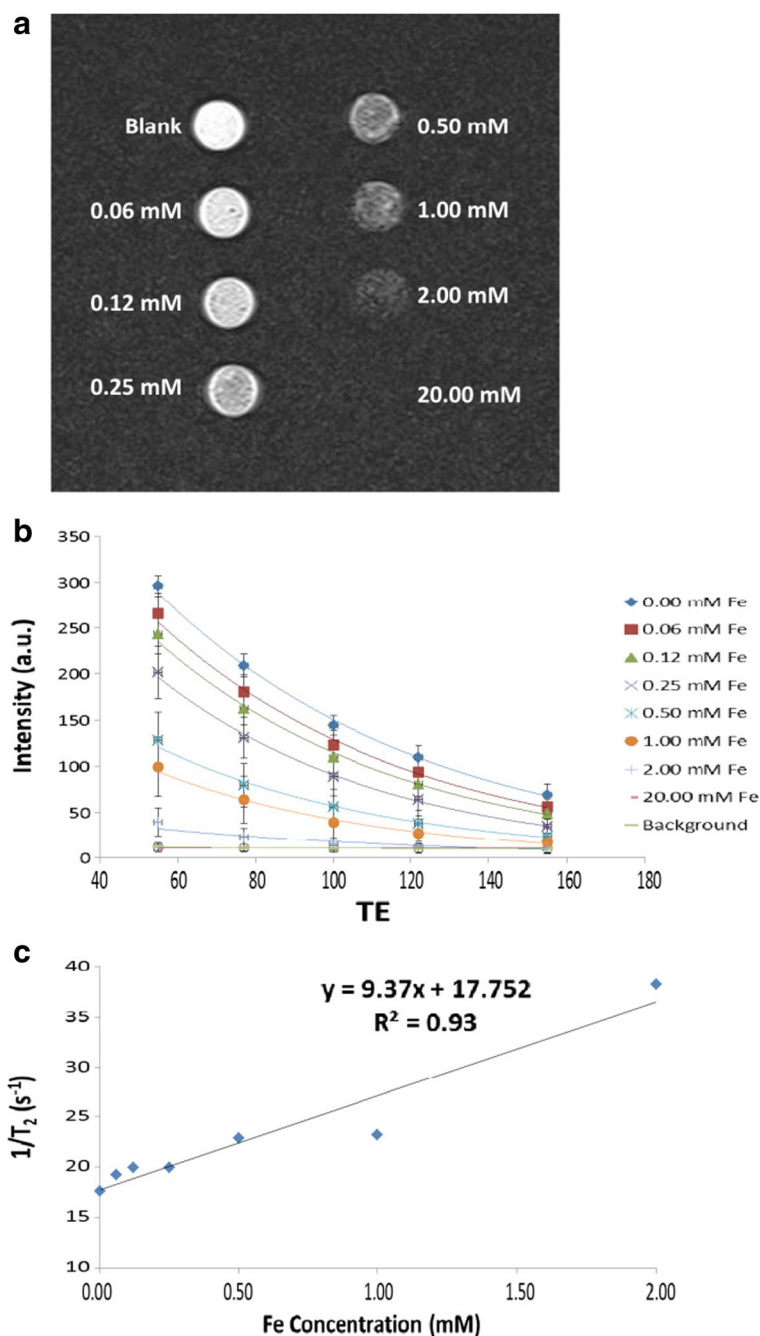
9c). This indicates that the DOX delivered by GO-CD, Fe@C, and GO-CD/Fe@C nanocarriers localized mainly in the nucleus, with some amount remaining in the cytoplasm. In addition, FGA-labeled GO-CD was found to remain in the cytoplasm under high-content screening (data not shown). This suggested that the DOX is released from the nanohybrids upon cellular uptake and diffused to the nucleus. A similar finding was also reported in our previous publication on DOX-loaded diblock copolymer micelles with pendant Dendron (Viswanathan et al. 2016). The localization of DOX in the nuclei is vital to enable DOX to interact with DNA through intercalation, which
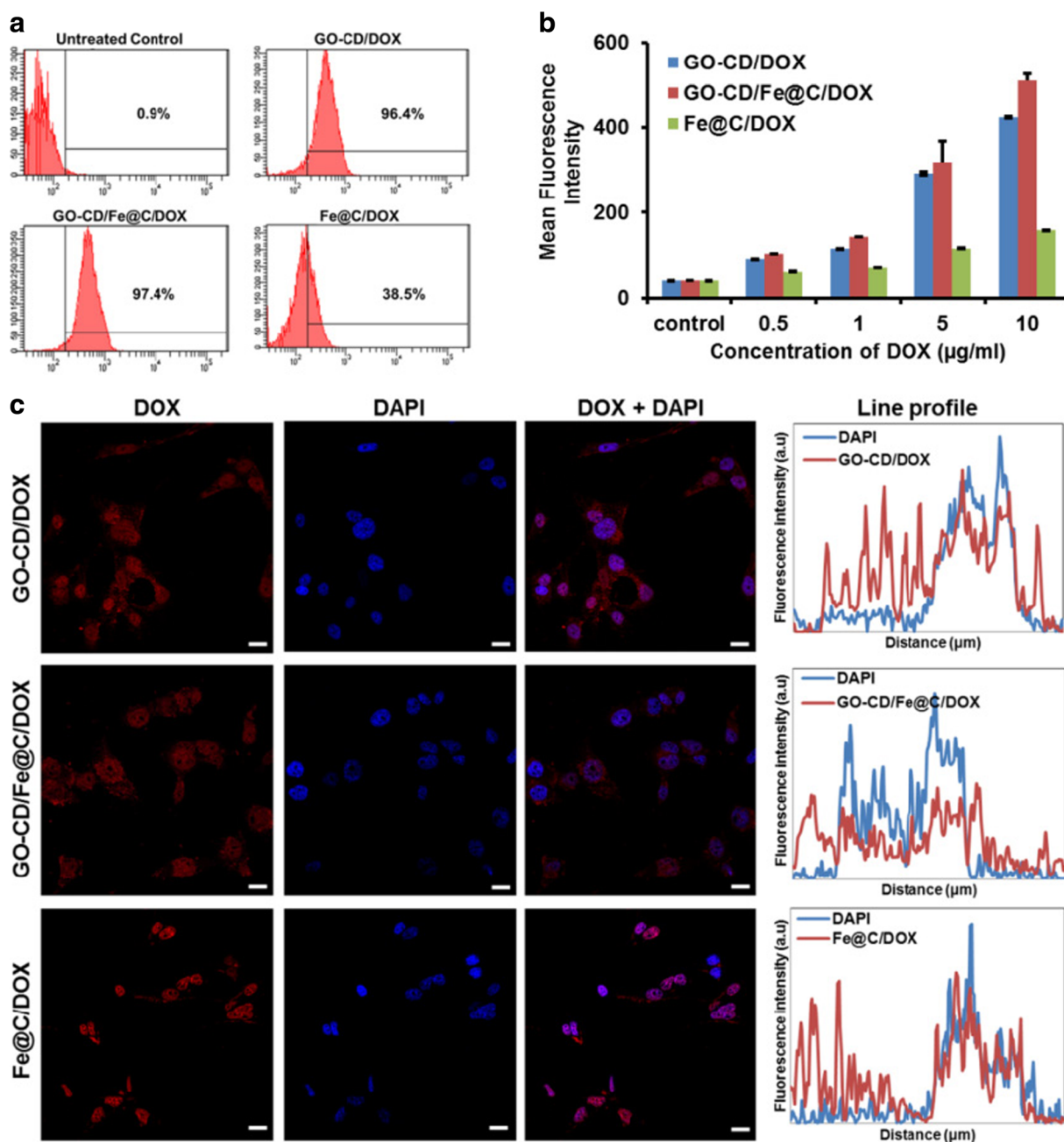
Fig. 9 Cellular uptake of nanocarriers loaded with DOX (10 μg/ml) in MDA-MB-231 cells after 2 h incubation. **a** Percentage cellular uptake for nanocarriers/DOX by flow cytometry. Concentration of DOX = 10 μg/ml. **b** Mean fluorescence intensity of nanocarriers/DOX in cells from flow cytometry data. Data are expressed as the mean ± SD ($n = 3$). **c** Confocal microscopic images and line profiles of nanocarriers/DOX. Scale bar, 20 μm

causes the disruption of topoisomerase-II-mediated DNA repair. This prevents the DNA double helix from being resealed after unwinding for replication, and leads to DNA damage and cell death (Thorn et al. 2011; Viswanathan et al. 2016).

Energy-dependent cellular uptake study

The MDA-MB-231 cells were treated with GO-CD/DOX, GO-CD-Fe@C/DOX, and Fe@C/DOX to determine the cellular uptake mechanism and intracellular

Fig. 10 Percentage of temperature-dependent cellular uptake (37 and 4 °C) for GO-CD/DOX, GO-CD/Fe@C/DOX, and Fe@C/DOX on 4T1 cells measured using flow cytometry. Data are represented as the mean ± SD ($n = 3$). Student's t test, *$p < 0.05$ compared to cellular uptake at 37 °C
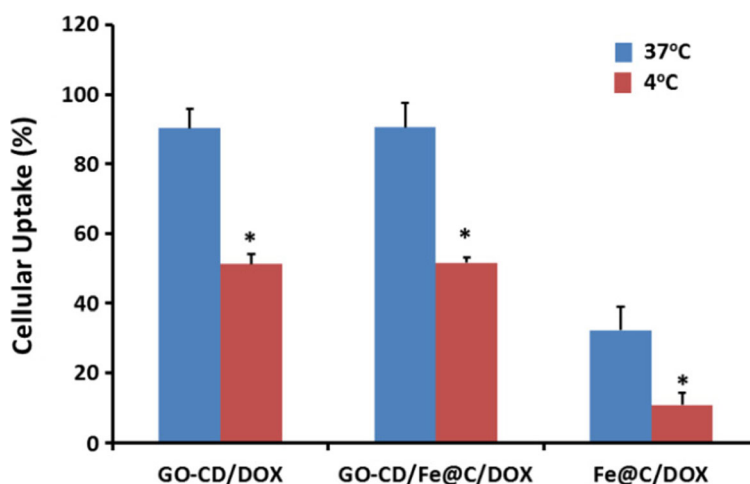
localization. The cellular internalization of various nanostructures mainly occurred via endocytosis.

Almost all endocytic pathways are energy-dependent processes that can be inhibited at low temperature, 4 °C (Kou et al. 2013; Thurn et al. 2011). Figure 10 shows that the incubation of the 4T1 cells with GO-CD/Fe@C/DOX and GO-CD/DOX at 4 °C for 2 h had caused an approximately 43% decrease in uptake compared with the cells incubated at 37 °C, as measured by flow cytometry (Fig. 10, Student's t test, $p < 0.05$). Meanwhile, approximately 66% decrease in cellular uptake was observed in Fe@C/DOX-treated cells when incubated at 4 °C.

A significant decrease in the cellular uptake of these nanocarriers at low temperature indicates that the internalization of the nanocarriers into 4T1 tumor cells is most likely to occur through energy-dependent endocytosis. Our finding concurs with our previous report in which the DOX-loaded micellar diblock copolymers were also internalized in the MDA-MB-231 cells via an energy-dependent process (Viswanathan et al. 2016).

Intracellular localization of GO-CD, Fe@C, and GO-CD/Fe@C nanocarriers

To determine the intracellular localization of GO-CD, Fe@C, and GO-CD/Fe@C nanocarriers in tumor cell, co-localization studies using LysoTracker (blue), ER-Tracker (blue), and MitoTracker (green) as the markers for lysosomes, endoplasmic reticulum, and mitochondria, respectively, were carried out and examined under a confocal microscope. The localization of the nanocarriers was determined based on the red fluorescence of DOX loaded in the carriers. The red fluorescence from DOX in GO-CD and GO-CD/Fe@C showed significant co-localization signal with MitoTracker, ER-Tracker, and LysoTracker, while the DOX in Fe@C nanocarrier showed co-localization with MitoTracker and LysoTracker and partially co-localized with the ER-Tracker (Fig. 11).

The current finding suggests that the GO-CD/Fe@C nanohybrid may be internalized into the MDA-MB-231 cells via endocytosis and localized in the lysosomes (Fig. 11a), which is the last compartment in the endocytic pathway. This finding is in agreement with a previous study suggesting that energy-dependent endocytosis can direct nanoparticles to lysosomal compartment (Chakraborty and Jana 2015).

In vitro cytotoxicity of DOX-loaded GO-CD, Fe@C, and GO-CD/Fe@C nanocarriers

DOX-loaded nanocarriers were examined for their cytotoxicity on MDA-MB-231 breast cancer cells using the MTT assay, and the IC_{50} values were evaluated. Both the GO-CD/DOX and GO-CD/Fe@C/DOX displayed a similar concentration-dependent increase of cytotoxicity, whereas Fe@C/DOX did not show significant toxicity effect (viability > 80%) after the treatment of cells for 24 h (Fig. 12a). This suggests that the conjugation of GO-CD to Fe@C had increased the

Fig. 11 Cellular uptake of nanocarrier/DOX on MDA-MB-231 cells co-stained with different organelle-specific trackers. **a** LysoTracker blue. **b** ER-Tracker blue. **c** MitoTracker green. Scale bar, 20 μm
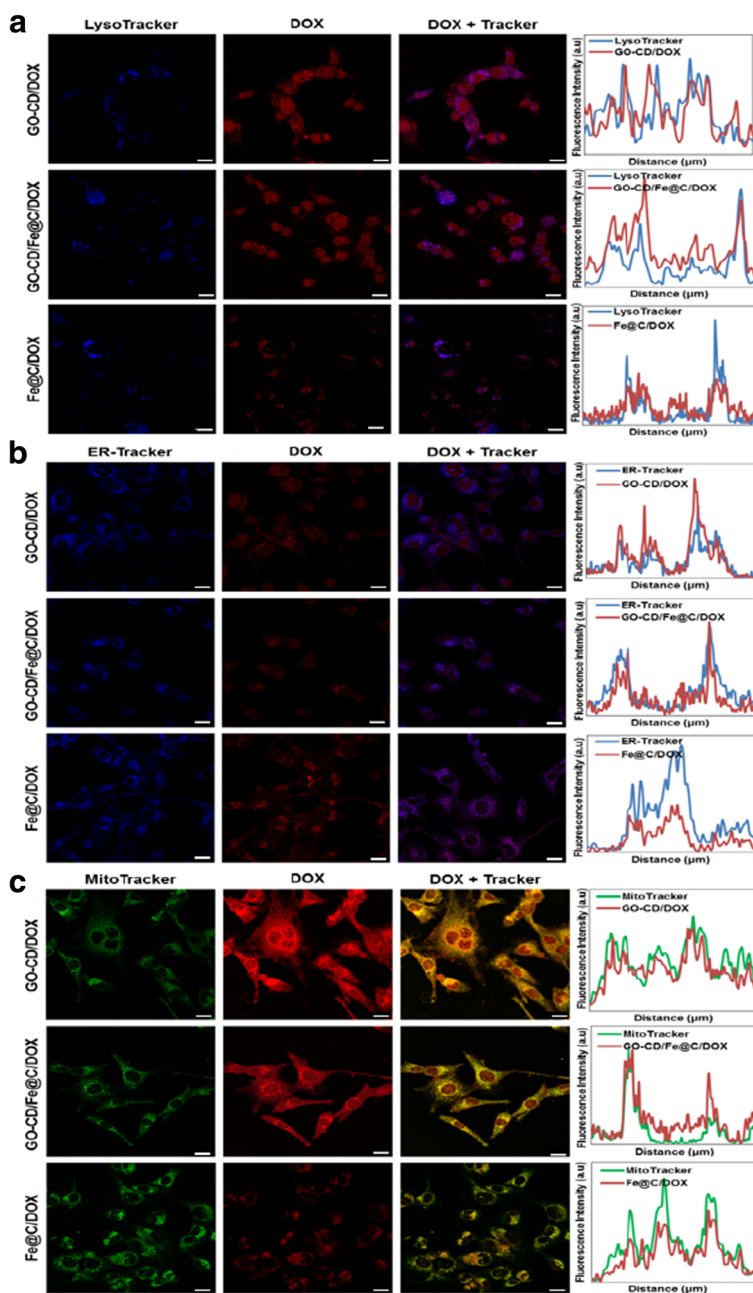
cellular uptake of DOX as discussed in the section above and, thus, enhanced the cytotoxicity of DOX loaded in GO-CD/Fe@C (GO-CD/Fe@C/DOX).

When the incubation time was increased to 48 h, the cytotoxicities of GO-CD/DOX and GO-CD/Fe@C/DOX were increased with a 10-fold lower IC_{50} value compared with those at 24 h incubation time (Fig. 12b and Table 4). Fe@C/DOX also exhibited significant cytotoxicity with an IC_{50} of 13.2 μg/ml DOX equivalent at the cell treatment for 48 h. This suggests that the cellular uptake of the nanocarriers is likely increased with time in a closed cell culture system. The decreasing order of cytotoxicity was as follows: GO-CD/DOX ≈ GO-CD/Fe@C/DOX > Fe@C/DOX. In
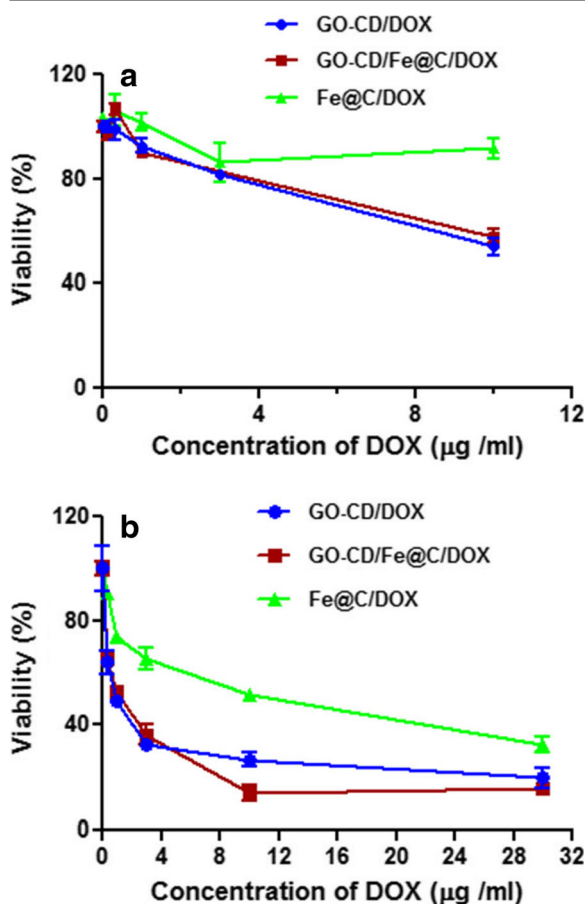
Fig. 12 The effect of nanocarriers loaded with DOX on the cell viability of MDA-MB-231 cells at 37 °C and at **a** 24 h and **b** 48 h of incubation. Data are represented as the mean ± SD ($n = 3$)

particular, IC$_{50}$ values of GO-CD/DOX and GO-CD/Fe@C/DOX at 48 h were within the range (from 0.025 to 2.7 μM DOX equivalent) of IC$_{50}$ previously reported for MDA-MB-231 cells (Aroui et al. 2009; Gouaze-Andersson et al. 2007; Shroff and Kokkoli 2012; Smith et al. 2006; Wu et al. 2013).

Table 4 IC$_{50}$ values (μg/ml) of DOX-loaded nanocarriers for MDA-MB-231 cancer cell after 24 and 48 h MTT assay treatments

Sample name	IC$_{50}$ (μg/ml)	
	24 h	48 h
Fe@C/DOX	79.2 ± 1.3	13.2 ± 0.05
GO-CD/DOX	10.0 ± 1.5	1.1 ± 0.06
GO-CD/Fe@C/DOX	12.2 ± 0.5	1.2 ± 0.04

Data are represented as the mean ± SD ($n = 3$)

These results suggest that the anticancer effects can be enhanced by increasing the tumor cellular uptake of DOX using GO-CD or GO-CD/Fe@C nanocarriers.

Conclusions

In summary, the designed nanohybrid consisting of graphene oxide-cyclodextrin (GO-CD) bound to carbon-coated iron (Fe@C) is a potential multifunctional nanocarrier that possesses high drug loading capacity and superparamagnetic property for magnetic-directed anticancer drug delivery and magnetic resonance imaging. The functionalization of CD on the GO and carbon coating on the Fe@C had enhanced the adsorption of DOX that results in a cumulative increase in the amount DOX entrapped in the nanohybrid. The GO-CD/Fe@C/DOX also demonstrated a higher amount of drug release in an acidic tumor environment compared to the amount of drug released at physiological pH. Increased cellular uptake of DOX in MDA-MD-231 breast tumor cells by 2.5-fold was observed when DOX was delivered using GO-CD/Fe@C nanohybrid as compared to Fe@C. This also resulted in significant cytotoxicity found in tumor cells treated with GO-CD/Fe@C/DOX. These findings strongly indicate that GO-CD/Fe@C nanohybrid is a promising multifunctional carrier for anticancer drug delivery.

In addition, the Fe@C component could further enhance the tumor selectivity and increase uptake of anticancer drug by tumor cells when a magnetic field is applied to direct and retain the nanohybrids at the tumor sites (Fernández-Pacheco et al. 2005). Additionally, Fe@C possesses superparamagnetic property as magnetic resonance contrast agent. We believe that these characteristics may enable the use of GO-CD/Fe@C nanohybrid as a "theranostic" agent for tumor detection and treatment and to assess therapeutic effects in clinics (Thomas et al. 2015).

Compliance with ethical standards

Conflict of interest The authors declare that they have no competing interest.

References

Aguiló-Aguayo N, Inestrosa-Izurieta M, García-Céspedes J, Bertran E (2010) Morphological and magnetic properties of superparamagnetic carbon-coated Fe nanoparticles produced by arc discharge. J Nanosci Nanotechnol 10:2646–2649. https://doi.org/10.1166/jnn.2010.1420

Alexiou C, Arnold W, Klein RJ, Parak FG, Hulin P, Bergemann C, Erhardt W, Wagenpfeil S, Lubbe AS (2000) Locoregional cancer treatment with magnetic drug targeting. Cancer Res 60:6641–6648

Aroui S, Ram N, Appaix F, Ronjat M, Kenani A, Pirollet F, De Waard M (2009) Maurocalcine as a non toxic drug carrier overcomes doxorubicin resistance in the cancer cell line MDA-MB 231. Pharm Res 26:836–845. https://doi.org/10.1007/s11095-008-9782-1

Bae H, Ahmad T, Rhee I, Chang Y, Jin SU, Hong S (2012) Carbon-coated iron oxide nanoparticles as contrast agents in magnetic resonance imaging. Nanoscale Res Lett 7:44. https://doi.org/10.1186/1556-276x-7-44

Bandara NA, Hansen MJ, Low PS (2014) Effect of receptor occupancy on folate receptor internalization. Mol Pharm 11:1007–1013. https://doi.org/10.1021/mp400659t

Brumlik MJ, Daniel BJ, Waehler R, Curiel DT, Giles FJ, Curiel TJ (2008) Trends in immunoconjugate and ligand-receptor based targeting development for cancer therapy. Expert Opin Drug Deliv 5:87–103. https://doi.org/10.1517/17425247.5.1.87

Busquets J, Del Galdo F, Kissin EY, Jimenez SA (2010) Assessment of tissue fibrosis in skin biopsies from patients with systemic sclerosis employing confocal laser scanning microscopy: an objective outcome measure for clinical trials? Rheumatology (Oxford, England) 49:1069–1075. https://doi.org/10.1093/rheumatology/keq024

Chakraborty A, Jana NR (2015) Clathrin to lipid raft-endocytosis via controlled surface chemistry and efficient perinuclear targeting of nanoparticle. J Phys Chem Lett 6:3688–3697. https://doi.org/10.1021/acs.jpclett.5b01739

Chomoucka J, Drbohlavova J, Huska D, Adam V, Kizek R, Hubalek J (2010) Magnetic nanoparticles and targeted drug delivering. Pharmacol Res 62:144–149. https://doi.org/10.1016/j.phrs.2010.01.014

Cortés-Funes H, Coronado C (2007) Role of anthracyclines in the era of targeted therapy. Cardiovasc Toxicol 7:56–60. https://doi.org/10.1007/s12012-007-0015-3

Das M, Mohanty C, Sahoo SK (2009) Ligand-based targeted therapy for cancer tissue. Expert Opin Drug Deliv 6:285–304. https://doi.org/10.1517/17425240902780166

Fan J, Park H, Tan S, Lee M (2013) Enhanced osteogenesis of adipose derived stem cells with Noggin suppression and delivery of BMP-2. PLoS One 8:e72474. https://doi.org/10.1371/journal.pone.0072474

Fernández-Pacheco R, Ibarra MR, Valdivia JG, Marquina C, Serrate D, Romero MS (2005) Carbon coated magnetic nanoparticles for local drug delivery using magnetic implants. NanoBiotechnology 1:300–303. https://doi.org/10.1007/s12030-005-0051-7

Gouaze-Andersson V, Yu JY, Kreitenberg AJ, Bielawska A, Giuliano AE, Cabot MC (2007) Ceramide and glucosylceramide upregulate expression of the multidrug resistance gene MDR1 in cancer cells. Biochim Biophys Acta 1771:1407–1417. https://doi.org/10.1016/j.bbalip.2007.09.005

Himaja A, Karthik P, Singh SP (2015) Carbon dots: the newest member of the carbon nanomaterials family. Chem Rec 15:595–615. https://doi.org/10.1002/tcr.201402090

Hubbell JA, Chilkoti A (2012) Nanomaterials for drug delivery. Science 337:303–305. https://doi.org/10.1126/science.1219657

Jusin JW, Aziz M, Sean GP, Jaafar J (2016) Preparation and characterization of graphene-based magnetic hybrid nanocomposite. Malaysian J Anal Sci 20:149–156. 10.17576/mjas-2016-2001-16

Kiew SF, Kiew LV, Lee HB, Imae T, Chung LY (2016) Assessing biocompatibility of graphene oxide-based nanocarriers: a review. J Control Release 226:217–228. https://doi.org/10.1016/j.jconrel.2016.02.015

Kobayashi T, Kakimi K, Nakayama E, Jimbow K (2014) Antitumor immunity by magnetic nanoparticle-mediated hyperthermia. Nanomed 9:1715–1726. https://doi.org/10.2217/nnm.14.106

Konkena B, Vasudevan S (2012a) Covalently linked, water-dispersible, cyclodextrin: reduced-graphene oxide sheets. Langmuir 28:12432–12437. https://doi.org/10.1021/la3020783

Konkena B, Vasudevan S (2012b) Understanding aqueous dispersibility of graphene oxide and reduced graphene oxide through pKa measurements. J Phys Chem Lett 3:867–872. https://doi.org/10.1021/jz300236w

Kou L, Sun J, Zhai Y, He Z (2013) The endocytosis and intracellular fate of nanomedicines: implication for rational design. Asian J Pharm Sci 8:1–10. https://doi.org/10.1016/j.ajps.2013.07.001

Krishnakumar B, Imae T, Miras J, Esquena J (2014) Synthesis and azo dye photodegradation activity of ZrS 2–ZnO nano-composites. Sep Purif Technol 132:281–288. https://doi.org/10.1016/j.seppur.2014.05.018

Kue CS, Kamkaew A, Burgess K, Kiew LV, Chung LY, Lee HB (2016) Small molecules for active targeting in cancer. Med Res Rev 36:494–575. https://doi.org/10.1002/med.21387

Liu G, Shen H, Mao J, Zhang L, Jiang Z, Sun T, Lan Q, Zhang Z (2013) Transferrin modified graphene oxide for glioma-targeted drug delivery: in vitro and in vivo evaluations. ACS Appl Mater Interfaces 5:6909–6914. https://doi.org/10.1021/am402128s

Liu Z, Robinson JT, Sun X, Dai H (2008) PEGylated nanographene oxide for delivery of water-insoluble cancer drugs. J Am Chem Soc 130:10876–10877. https://doi.org/10.1021/ja803688x

Ma X, Tao H, Yang K, Feng L, Cheng L, Shi X, Li Y, Guo L, Liu Z (2012) A functionalized graphene oxide-iron oxide nanocomposite for magnetically targeted drug delivery, photothermal therapy, and magnetic resonance imaging. Nano Res 5:199–212. https://doi.org/10.1007/s12274-012-0200-y

Mahajan S, Koul V, Choudhary V, Shishodia G, Bharti AC (2013) Preparation and in vitro evaluation of folate-receptor-targeted SPION-polymer micelle hybrids for MRI contrast enhancement in cancer imaging. Nanotechnology 24:015603. https://doi.org/10.1088/0957-4484/24/1/015603

Mody VV, Cox A, Shah S, Singh A, Bevins W, Parihar H (2013) Magnetic nanoparticle drug delivery systems for targeting tumor. Appl Nanosci 4:385–392. https://doi.org/10.1007/s13204-013-0216-y

Narayanan T, Liu Z, Lakshmy PR, Gao W, Nagaoka Y, Kumar DS, Lou J, Vajtai R, Ajayan PM (2012) Synthesis of reduced graphene oxide–Fe 3 O 4 multifunctional freestanding membranes and their temperature dependent electronic transport properties. Carbon 50:1338–1345. https://doi.org/10.1016/j.carbon.2011.11.005

Nawara K, Romiszewski J, Kijewska K, Szczytko J, Twardowski A, Mazur M, Krysinski P (2012) Adsorption of doxorubicin onto citrate-stabilized magnetic nanoparticles. J Phys Chem C 116:5598–5609. https://doi.org/10.1021/jp2095278

Ohashi H, Hiraoka Y, Yamaguchi T (2006) An autonomous phase transition−complexation/decomplexation polymer system with a molecular recognition property. Macromolecules 39:2614–2620. https://doi.org/10.1021/ma052509q

Paredes JI, Villar-Rodil S, Martínez-Alonso A, Tascón JMD (2008) Graphene oxide dispersions in organic solvents. Langmuir 24:10560–10564. https://doi.org/10.1021/la801744a

Paulos CM, Reddy JA, Leamon CP, Turk MJ, Low PS (2004) Ligand binding and kinetics of folate receptor recycling in vivo: impact on receptor-mediated drug delivery. Mol Pharmacol 66:1406–1414. https://doi.org/10.1124/mol.104.003723

Popplewell J, Sakhnini L (1995) The dependence of the physical and magnetic properties of magnetic fluids on particle size. J Magn Magn Mater 149:72–78. https://doi.org/10.1016/0304-8853(95)00341-X

Prasannan A, Imae T (2013) One-pot synthesis of fluorescent carbon dots from orange waste peels. Ind Eng Chem Res 52:15673–15678. https://doi.org/10.1021/ie402421s

Rosická D, Šembera J (2011) Influence of structure of iron nanoparticles in aggregates on their magnetic properties. Nanoscale Res Lett 6:527. https://doi.org/10.1186/1556-276X-6-527

Rudge SR, Kurtz TL, Vessely CR, Catterall LG, Williamson DL (2000) Preparation, characterization, and performance of magnetic iron–carbon composite microparticles for chemotherapy. Biomaterials 21:1411–1420. https://doi.org/10.1016/S0142-9612(00)00006-5

Shen J, Hu Y, Shi M, Li N, Ma H, Ye M (2010) One step synthesis of graphene oxide−magnetic nanoparticle composite. J Phys Chem C 114:1498–1503. https://doi.org/10.1021/jp909756r

Shi J, Wang L, Zhang J, Ma R, Gao J, Liu Y, Zhang C, Zhang Z (2014) A tumor-targeting near-infrared laser-triggered drug delivery system based on GO@Ag nanoparticles for chemo-photothermal therapy and X-ray imaging. Biomaterials 35:5847–5861. https://doi.org/10.1016/j.biomaterials.2014.03.042

Shroff K, Kokkoli E (2012) PEGylated liposomal doxorubicin targeted to alpha5beta1-expressing MDA-MB-231 breast cancer cells. Langmuir 28:4729–4736. https://doi.org/10.1021/la204466g

Siriviriyanun A, Popova M, Imae T, Kiew LV, Looi CY, Wong WF, Lee HB, Chung LY (2015) Preparation of graphene oxide/dendrimer hybrid carriers for delivery of doxorubicin. Chem Eng J 281:771–781. https://doi.org/10.1016/j.cej.2015.07.024

Smith L, Watson MB, O'Kane SL, Drew PJ, Lind MJ, Cawkwell L (2006) The analysis of doxorubicin resistance in human breast cancer cells using antibody microarrays. Mol Cancer Ther 5:2115–2120. https://doi.org/10.1158/1535-7163.mct-06-0190

Sun Y-P, Li X-q, Cao J, Zhang W-x, Wang HP (2006) Characterization of zero-valent iron nanoparticles. Adv Colloid Interf Sci 120:47–56. https://doi.org/10.1016/j.cis.2006.03.001

Tannock IF, Rotin D (1989) Acid pH in tumors and its potential for therapeutic exploitation. Cancer Res 49:4373–4384

Terzyk AP (2001) The influence of activated carbon surface chemical composition on the adsorption of acetaminophen (paracetamol) in vitro: part II. TG, FTIR, and XPS analysis of carbons and the temperature dependence of adsorption kinetics at the neutral pH. Colloids Surf Physicochem Eng Aspects 177:23–45. https://doi.org/10.1016/S0927-7757(00)00594-X

Thomas RG, Moon MJ, Lee H, Sasikala AR, Kim CS, Park IK, Jeong YY (2015) Hyaluronic acid conjugated superparamagnetic iron oxide nanoparticle for cancer diagnosis and hyperthermia therapy. Carbohydr Polym 131:439–446. https://doi.org/10.1016/j.carbpol.2015.06.010

Thorn CF, Oshiro C, Marsh S, Hernandez-Boussard T, McLeod H, Klein TE, Altman RB (2011) Doxorubicin pathways: pharmacodynamics and adverse effects. Pharmacogenet Genomics 21:440–446. https://doi.org/10.1097/FPC.0b013e32833ffb56

Thurn KT, Arora H, Paunesku T, Wu A, Brown EMB, Doty C, Kremer J, Woloschak G (2011) Endocytosis of titanium dioxide nanoparticles in prostate cancer PC-3M cells. Nanomed Nanotechnol 7:123–130. https://doi.org/10.1016/j.nano.2010.09.004

Tourinho F, Franck R, Massart R, Perzynski R (1989) Synthesis and mangeitc properties of managanese and cobalt ferrite ferrite ferrofluids. In: Bothorel P, Dufourc EJ (eds) Trends in colloid and Interface science III. Steinkopff, Darmstadt, pp 128–134. https://doi.org/10.1007/BFb0116198

Vermisoglou E, Devlin E, Giannakopoulou T, Romanos G, Boukos N, Psycharis V, Lei C, Lekakou C, Petridis D, Trapalis C (2014) Reduced graphene oxide/iron carbide nanocomposites for magnetic and supercapacitor applications. J Alloys Compd 590:102–109. https://doi.org/10.1016/j.jallcom.2013.11.087

Viswanathan G, Hsu Y-H, Voon SH, Imae T, Siriviriyanun A, Lee HB, Kiew LV, Chung LY, Yusa S-I (2016) A comparative study of cellular uptake and subcellular localization of doxorubicin loaded in self-assemblies of amphiphilic copolymers with pendant Dendron by MDA-MB-231 human breast cancer cells. Macromol Biosci 16:882–895. https://doi.org/10.1002/mabi.201500435

Voon SH, Kiew LV, Lee HB, Lim SH, Noordin MI, Kamkaew A, Burgess K, Chung LY (2014) In vivo studies of nanostructure-based photosensitizers for photodynamic cancer therapy. Small 10:4993–5013. https://doi.org/10.1002/smll.201401416

Wang C, Li B, Niu W, Hong S, Saif B, Wang S, Dong C, Shuang S (2015a) β-Cyclodextrin modified graphene oxide–magnetic nanocomposite for targeted delivery and pH-sensitive release of stereoisomeric anti-cancer drugs. RSC Adv 5:89299–89308. https://doi.org/10.1039/C5RA13082D

Wang Q, Zhou L, Qiu L, Lu D, Wu Y, Zhang X-B (2015b) An efficient ratiometric fluorescent probe for tracking dynamic changes in lysosomal pH. Analyst 140:5563–5569. https://doi.org/10.1039/C5AN00683J

Wu A, Loutherback K, Lambert G, Estévez-Salmerón L, Tlsty TD, Austin RH, Sturm JC (2013) Cell motility and drug gradients in the emergence of resistance to chemotherapy. Proc Natl Acad Sci U S A 110:16103–16108. https://doi.org/10.1073/pnas.1314385110

Yang X, Wang Y, Huang X, Ma Y, Huang Y, Yang R, Duan H, Chen Y (2011) Multi-functionalized graphene oxide based anticancer drug-carrier with dual-targeting function and pH-sensitivity. J Mater Chem 21:3448–3454. https://doi.org/10.1039/C0JM02494E

Yu D, Yang Y, Durstock M, Baek J-B, Dai L (2010) Soluble P3HT-grafted graphene for efficient bilayer−heterojunction photovoltaic devices. ACS Nano 4:5633–5640. https://doi.org/10.1021/nn101671t

Zhang L, Xia J, Zhao Q, Liu L, Zhang Z (2010) Functional graphene oxide as a nanocarrier for controlled loading and targeted delivery of mixed anticancer drugs. Small 6:537–544. https://doi.org/10.1002/smll.200901680